Electron beam synthesis of metal and semiconductor nanoparticles using metal–organic frameworks as ordered precursors

2011 Nanotechnology 22 375601

(http://iopscience.iop.org/0957-4484/22/37/375601)

Nanotechnology **22** (2011) 375601 (6pp) doi:10.1088/0957-4484/22/37/375601

Electron beam synthesis of metal and semiconductor nanoparticles using metal–organic frameworks as ordered precursors

Benjamin W Jacobs[1], Ronald J T Houk[1], Bryan M Wong[1], A Alec Talin[2] and Mark D Allendorf[1]

[1] Sandia National Laboratories, 7011 East Avenue, Livermore, CA, USA
[2] National Institute of Standards and Technology, 100 Bureau Avenue, Gaithersburg, MD, USA

E-mail: mdallen@sandia.gov

Received 18 May 2011, in final form 16 July 2011
Published 18 August 2011
Online at stacks.iop.org/Nano/22/375601

Abstract
We demonstrate a versatile, bottom-up method of forming metal and semiconducting nanoparticles by exposing precursor metal–organic frameworks (MOFs) to an electron beam. Using a transmission electron microscope to initiate and observe growth, we show that the composition, size, and morphology of the nanoparticles are determined by the chemistry and structure of the MOF, as well as the electron beam properties. Zinc oxide, metallic indium and copper particles were produced with narrow and tunable size distributions comparable to those obtained from state-of-the-art methods. This method represents a first step toward the fabrication of nanoscale heterostructures using the highly controlled environment of the MOF pores as a scaffold or template.

S Online supplementary data available from stacks.iop.org/Nano/22/375601/mmedia

(Some figures in this article are in colour only in the electronic version)

The unique, size-dependent properties of metallic and semiconducting nanoparticles continue to generate enormous interest in using these materials for applications ranging from electronics to catalysis and bio/medicine [1–5]. A recent innovation that produces extremely small metallic particles was described by Fischer *et al*, in which metal–organic frameworks (MOFs) are infiltrated with organometallic precursors, then 'developed' using thermal, photolytic, or chemical reduction methods [6]. MOFs are crystalline materials composed of metal ions or clusters connected by organic ligands to create a rigid framework. This structure is advantageous as a template because it provides considerable flexibility to tune both pore size and chemical environment, and an extensive library of MOFs now exists. The nanoparticles resulting from MOF infiltration are on the order of the pore dimensions (typically <2 nm) and are chemically stabilized by the framework. We and others [7] extended this concept by using metal salts to create silver and gold nanoparticles as small as Ag_3 [8]. Unfortunately, since very few MOFs with pore sizes of $\geqslant 2.5$ nm exist, a wide range of potentially interesting particle sizes are inaccessible.

Here, we demonstrate an alternative approach in which the MOF itself is the precursor to particle formation. Recently, we showed that exposing silver-infiltrated MOF templates to an electron beam leads to rapid framework breakdown and subsequent Ag coalescence. Depending on the MOF structure, either nanoparticles in the 2–6 nm size range or arrays of nanowires can be created [8, 9]. Intriguingly, the metal ions composing the framework are captured within the amorphous decomposition matrix and do not form individual nanoparticles (for example, no Zn-containing particles are detected following exposure of Ag@MOF-508 to the electron beam). In this work, we advance this concept to show that electron beam (e-beam) decomposition of neat MOFs can be used to create both metal and metal-oxide nanoparticles. Although e-beams have been used to form nanoparticles [10, 11], nanowires [12],

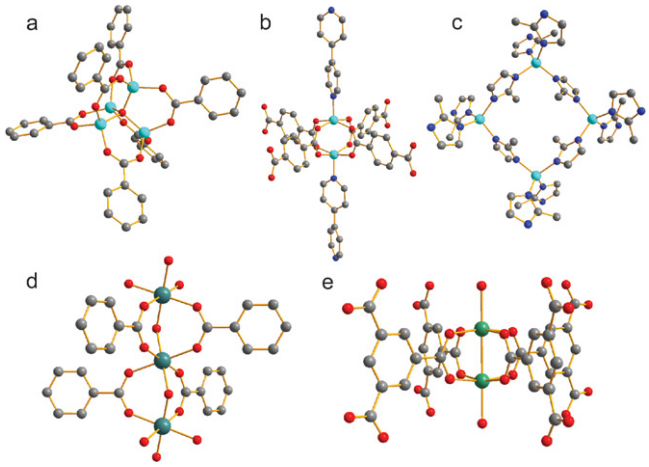

Figure 1. (a) IRMOF-1 SBU (IR isoreticular; SBU—secondary building unit). (b) MOF-508 SBU (c) ZIF-8 SBU (d) Cu(BTC) SBU (e) MIL-68(In) SBU. Gray: carbon; red: oxygen; aqua: zinc; blue: nitrogen; green: copper; teal: indium.

and modify the electrical properties of materials [13], the use of MOFs as precursors offers several important advantages. First, it eliminates processing steps associated with infiltrating MOF templates and avoids the use of highly reactive and toxic precursors. Second, since MOFs can be grown on surfaces [14], the extremely high spatial resolution afforded by e-beam methods, coupled with the highly ordered, well-defined MOF pore structure and unit cell dimensions, create the potential for bottom-up self-assembly and patterning of feature sizes in the single-digit nanometer range. Third, particle size can be controlled by varying the beam current, leading to particles as small as 1.2 nm with very narrow size distributions; larger particles (up to 100 nm) are also possible. Finally, the remaining carbonaceous linker material from the MOF acts as a matrix to prevent further coalescence, agglomeration, and oxidation. In this work we explore these concepts, using a transmission electron microscope (TEM) to both initiate nanoparticle self-assembly and obtain real time, *in situ* information concerning the nucleation, growth, and diffusion processes. The results provide not only proof-of-concept, but show that the mechanism of MOF decomposition, the particle composition, and the resulting particle morphology can be understood in terms of the atomic and nanoscale structure of the MOF, creating the potential for rational design.

The type and morphology of e-beam induced nanoparticles is determined by at least four factors: (1) the oxidation potential of the MOF metal centers; (2) the ligands in the coordination sphere surrounding the metal center and the strength of the bonds; (3) the coordination sphere geometry; and (4) the e-beam conditions. Five MOFs were used to systematically determine the influence of these parameters. The selected MOFs encompass a range of representative structures and chemistries. Three Zn-based MOFs, IRMOF-1, MOF-508 and ZIF-8 (figures 1(a)–(c)) were used to investigate the formation of Zn-based materials, such as ZnO, and to probe the effects of the coordination environment. IRMOF-1 has tetrahedral Zn_4O clusters connected by 1,4-benzenedicarboxylic acid (BDC, terephthalic acid) and enclosed pores [15]. MOF-508 has a mixed coordination sphere, in which 2D sheets are formed from Zn(II) ions in a paddlewheel arrangement, coordinated by BDC linkers in the plane and 4,4′-dipyridyl (bipy) pillar ligands perpendicular to the plane [16]. Finally, ZIF-8 (zeolitic imidazolate framework) has tetrahedral coordination by the nitrogens of imidazolate linkers, leading to a sodalite structure with enclosed pores [17]. The two remaining MOFs, indium-containing MOF MIL-68(In) and the copper-containing MOF Cu(BTC) (figures 1(d) and (e)), allow us to probe the dependence of the metal center and oxidation potential on the type of nanoparticles that form, while maintaining a carboxylate-based coordination sphere. MIL-68(In) is composed of infinite 1D chains of In atoms linked with BDC [18], and has open 1D channels. Cu(BTC), also known as HKUST-1, has a primitive cubic structure in which Cu(II) is coordinated to benzenetricarboxylic acid (BTC, trimesic acid) in a paddlewheel geometry, forming enclosed pores connected by smaller pore apertures [19]. The oxidation potentials of Cu(II) and In(III) are −0.34 eV and 0.34 eV versus standard hydrogen electrodes (SHE), respectively, compared with 0.76 eV versus SHE for Zn(II). The reduction potentials for Cu(II), In(III), and Zn(II) in their respective coordination environments found in the MOFs are not presently known. However, we can estimate these values using the reduction potentials measured for these ions in solutions of similar ligands: Zn(II)/acetate: −0.9 V versus SHE; Zn(II)/pyridine (in 0.1 M KCl): −0.8 V versus SHE; In(III)/citrate: −0.5 V versus SHE; and Cu(II)/citrate: −0.2 V versus SHE [20]. Thus, Cu and In in MOFs are expected to be more readily reduced to the metallic state than Zn. All MOF materials were synthesized as described in the literature (see supporting information available at stacks.iop.org/Nano/22/375601/mmedia).

Two TEMs operating in bright-field mode with different current densities and beam energies were used to initiate nanoparticle growth and observe the resulting nanoparticle morphology. A JEOL 2010F with a field emission source operating at 200 kV and a small beam current (1.03 mA cm^{-2}) was used to irradiate the MOFs, observe degradation in real time, and perform elemental analysis. The effect of higher current densities was probed using a JEOL 4000EX with a LaB_6 source operating at 400 kV. The current density is much

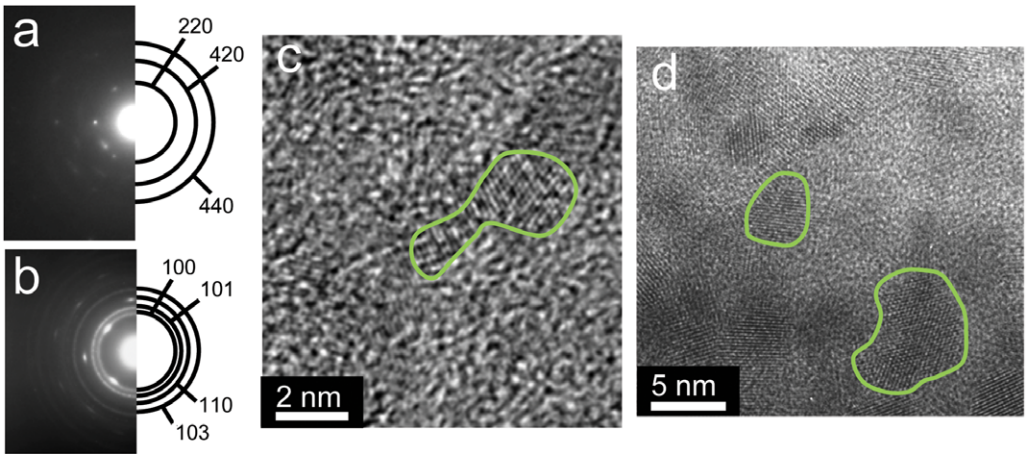

Figure 2. ZnO formation in IRMOF-1. (a) Electron diffraction pattern of the intact MOF. (b) Electron diffraction pattern of MOF after electron beam irradiation. This pattern corresponds to wurtzite ZnO. (c) HRTEM image of ZnO nanoparticles, a few examples of which are indicated by the green circles, embedded in the decomposed framework after irradiation in the 200 kV electron beam and (d) in the 400 kV electron beam.

higher in this instrument (73 mA cm^{-2}), but because of the higher accelerating voltage the actual energy deposition in the sample is lower by ≈22%, as determined from the Bethe equation [21].

The results of exposing the three Zn-based MOFs to the e-beam demonstrate that ZnO nanoparticles form and their size can be tuned using the e-beam current density. When IRMOF-1 is exposed to the 200 kV electron beam, ZnO nanoparticles readily form. As seen in figure 2(a), the SAED pattern of IRMOF-1 obtained after a few seconds in the beam indicates the MOF structure is intact for ≈30 s, due to the lower current density when the beam is defocused for this measurement. Under normal imaging conditions, however, the SAED pattern disappears after roughly 10 s, and after approximately 2 min ZnO nanoparticles are visible (figure 2(c)). These nanoparticles are consistently very small, on the order of 1 nm in diameter. A diffraction pattern could not be obtained for this sample, presumably because these particles are too small to significantly diffract. In contrast, after 60 s in the 400 kV beam, much larger, crystalline ZnO nanoparticles form, as shown by the SAED pattern corresponding to the wurtzite structure of ZnO (figure 2(b)). Spots in this pattern may indicate preferential growth directions or large single-crystal particles, but neither are directly observed. The post-exposure high-resolution TEM (HRTEM) image in figure 2(d) shows an array of 3–7 nm ZnO nanoparticles embedded in an amorphous matrix.

The IRMOF-1 transformation to ZnO is confirmed with micro-Raman and photoluminescence (PL) spectroscopy, collected before and after exposure to the 400 kV e-beam. The PL spectra of the unexposed and exposed IRMOF-1, as well as the neat BDC linker, are compared in figure S1 (available at stacks.iop.org/Nano/22/375601/mmedia). Weak bands visible in the luminescence spectrum of the exposed MOF correspond to the unexposed IRMOF-1 and BDC, indicating very little intact MOF remains. A new band is observed at 507 nm that is consistent with emission from deep-level traps from oxygen vacancies in nanocrystalline ZnO [22–24]. However, an accurate size distribution is difficult to obtain from the TEM images due to poor contrast. The composition of the amorphous matrix surrounding the particles is primarily elemental carbon, as indicated by micro-Raman spectroscopy (figure S2 available at stacks.iop.org/Nano/22/375601/mmedia). Vibrational modes seen in the linker and unexposed MOF spectra are not present in the spectrum of the exposed sample, but the broad peaks at 1345 cm^{-1} and 1606 cm^{-1} are attributed to amorphous and graphite-like carbon, respectively [25]. This carbonaceous material evidently serves as a stabilizing matrix, preventing further coalescence and agglomeration of the nanoparticles. Electron dispersive x-ray spectroscopy (EDS) done in the TEM indicates that Zn and O are also present, but we cannot determine whether these are incorporated into the carbon matrix or exist as a separate, amorphous ZnO phase.

Comparing the e-beam behavior of IRMOF-1 with the other two zinc-containing MOFs demonstrates the crucial role of the metal coordination sphere in determining whether or not nanoparticles form, and shows that nanoparticle growth conditions can be tuned using different linkers. In contrast to IRMOF-1, no ZnO is observed when MOF-508 is exposed to the 200 kV e-beam for any length of time. However, using the higher current densities available in the 400 kV e-beam, ZnO nanoparticles can be formed. The energy of the electrons in both TEM e-beams will initially ionize the materials along the electron track, after which the local excitation decays through various thermal and non-thermal routes to the ground state. The behaviors of the two MOFs indicate that the MOF-508 structure is more stable with respect to this excitation than IRMOF-1. In both MOFs Zn(II) is coordinated to four oxygen ions. The coordination geometry in IRMOF-1 (tetrahedral) is similar to the wurtzite ZnO structure. In MOF-508, the Zn(II) has a square-pyramidal paddlewheel configuration and is also coordinated to nitrogen from the bipy linker. We therefore speculate that the greater stability of MOF-508 results from a combination of the additional energy required to rearrange the coordination sphere to create ZnO and improved radical stability as a result of the polycyclic bipy linker.

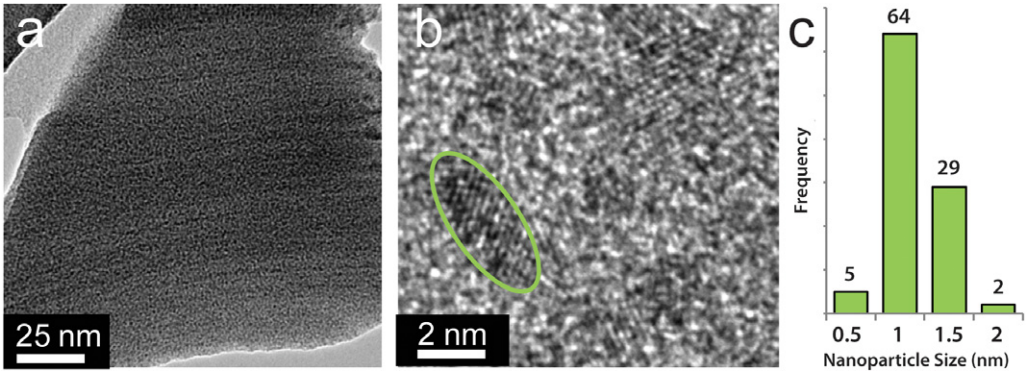

Figure 3. Indium nanoparticle formation in MIL-68(In). (a) TEM image of In nanoparticles embedded in the decomposed framework. Dark contrast spots are the nanoparticles. (b) HRTEM image of (a). Nanoparticles of In can be seen, indicated by the green circle. (c) Size distribution histogram of the as formed In nanoparticles.

It is conceivable that nanoparticles of other zinc-containing compounds could also form; both zinc nitride (Zn_3N_2; cubic) and carbide (ZnC) are known. However, exposing the nitrogen-only coordination sphere of ZIF-8 to both the 200 and 400 kV e-beams produces no detectable nanoparticles. Although it is possible these compounds could form in an amorphous state that is difficult to detect, it is also plausible that the low reactivity of the imidazole linker and/or the instability of Zn_3N_2 (known to react violently with water) prevent the formation of phases other than ZnO.

In addition to the coordination sphere, the oxidation potential of the MOF metal ions determines whether an oxide or a metal nanoparticle will form, as illustrated in MIL-68(In) and Cu(BTC). In these structures, the metal ions are surrounded by sufficient oxygen to create stoichiometric indium and copper oxides. Instead, these materials decompose to form the corresponding metal nanoparticles upon e-beam exposure. Traces of indium oxide are detected in the exposed MIL-68(In), but no copper oxides are found in the exposed Cu(BTC). This behavior is straightforwardly explained by the oxidation potentials of the three metals, as discussed above. Zn has the highest oxidation potential and is also one of the highest of any transition metal. It is therefore not surprising that in the presence of oxygen the nanoparticles derived from this growth method are ZnO. On the other hand, Cu has a much lower oxidation potential, favoring the formation of Cu nanoparticles. The structure of Cu(BTC) may also be advantageous, since two Cu atoms exist in close proximity in the paddlewheel structure. Indium has an oxidation potential intermediate to Cu and Zn. This evidently allows In_2O_3 to form in small quantities, but EDS indicates this exists only as a surface layer (figure S5 available at stacks.iop.org/Nano/22/375601/mmedia), in agreement with previous findings [26]. These results suggest that a relatively sharp boundary in oxidation potential separates the formation of metallic and oxide nanoparticles.

Cu(BTC) is very unstable in the beam, decomposing after 1–2 s, too short to obtain SAED patterns. Within 3–5 s in the 200 kV e-beam, Cu nanoparticles form with an average size of 2.7 nm $\pm$ 0.5 nm (figure S4 available at stacks.iop.org/Nano/22/375601/mmedia). These are among the smallest Cu nanoparticles with the narrowest size distribution reported to date [27]. Exposure to the 400 kV electron beam facilitates the formation of much larger nanoparticles by imparting more energy into the framework as a result of the higher current densities delivered by the LaB_6 electron gun relative to the 200 kV field emission electron gun. A TEM image following a 30 s exposure reveals particles as large as 60 nm in diameter (figure S4 available at stacks.iop.org/Nano/22/375601/mmedia).

MIL-68(In) is similar to Cu(BTC), breaking down very quickly and forming In nanoparticles within 3–5 s when exposed to the 200 kV electron beam. These particles are extremely small and nearly monodisperse, having an average diameter of 1.2 nm $\pm$ 0.3 nm, making them also among the smallest reported (figure 3). The nanoparticle size distributions were measured using bright-field images. Phase contrast images (figure (b)) were not used as the nanoparticles were not easily visible due to poor contrast. For non-spherical particles the width and length were averaged. Up to 100 nanoparticles were measured to obtain a good statistical distribution of particle sizes (this method was used to obtain all size distributions reported here).

When MIL-68(In) is exposed to the higher current density of the 400 kV beam, In nanoparticles with diameters as large as 100 nm form (figure 4(a)). Although the size distribution is broader than that of the much smaller nanoparticles discussed earlier, this observation suggests that beam current can be used to adjust particle size. HRTEM indicates that amorphous (figure 4(b)), polycrystalline, and single-crystal (figure 4(c)) morphologies are formed, as well as mixtures of these. Amorphous particles such as the one in figure 4(b) also have an amorphous shell (indicated by the spots and ring pattern in the fast Fourier transform), which could be either In, as previously reported [26], or carbonaceous material. An unexpected finding is that these large In nanoparticles, which lack any obvious grain boundaries, are composed of both face-centered cubic (fcc) and body-centered tetragonal (bct) phases. It is known that the crystal structure of In nanoparticles depends on size. Nanoparticles $<$10 nm in diameter have an fcc structure [26, 28, 29], which due to its higher symmetry is more stable at the nanoscale [26]. Nanoparticles of $>$10 nm diameter have the bulk bct structure. Nanobeam diffraction (NBD) analysis of individual nanoparticles clearly indicates

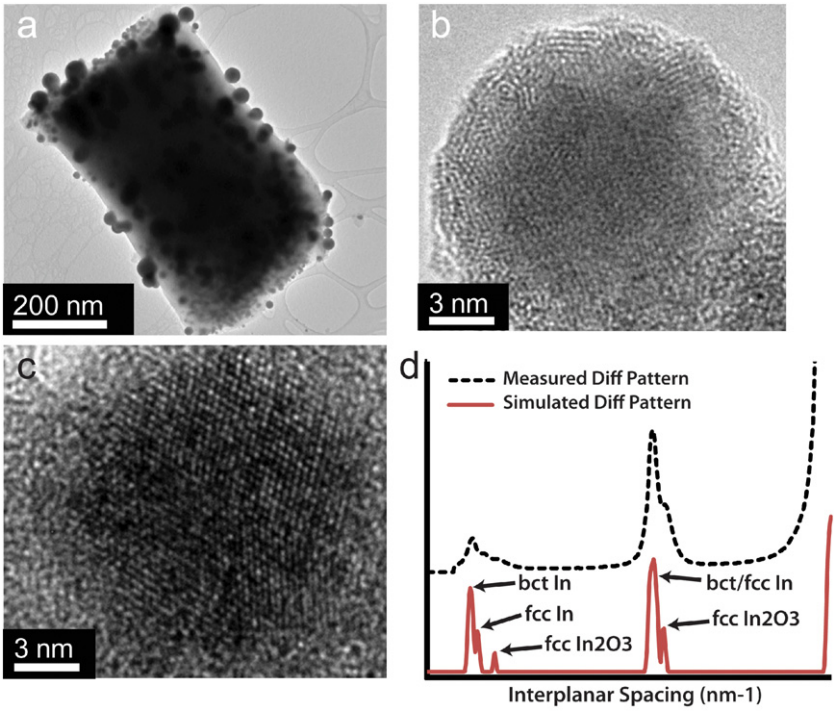

Figure 4. TEM images and measured and simulated diffraction patterns of In nanoparticles. (a) Larger nanoparticles, up to 100 nm in diameter, of In (dark contrast spots) form in the 400 kV electron beam. (b) HRTEM image of polycrystalline/amorphous In nanoparticle. (c) HRTEM image of a crystalline nanoparticle. Inset shows an FFT of the nanoparticle. (d) Intensity map of simulated and measured diffraction patterns (shown in supporting information available at stacks.iop.org/Nano/22/375601/mmedia).

that both fcc and bct phases are present in these particles (figure S6 available at stacks.iop.org/Nano/22/375601/mmedia). The intensities of the diffraction spots in simulated and measured diffraction patterns (figure S6 available at stacks.iop.org/Nano/22/375601/mmedia) are compared in figure 4(d). Reflections for fcc and bct phases nearly overlap, but are distinguishable, along with some In_2O_3. Unfortunately, NBD cannot reliably indicate the relative amounts of these phases, but the fact that the fct phase is detected at all indicates that these domains are not the result of a minor impurity. As such, to our knowledge these are the largest fcc-In nanoparticles reported. The fact that this crystal structure is normally found in nanoparticles at least ten times smaller suggests that coalescence is sufficiently rapid under these conditions for metastable crystal phases to form (see supporting information for more details available at stacks.iop.org/Nano/22/375601/mmedia).

The e-beam induced breakdown of MOFs very likely proceeds by a mechanism similar to that in organic materials, which is attributed to bond scission by means of secondary electron generation [30]. Localized heating plays essentially no role, as the temperature increase predicted by the Bethe equation is less than 10 K [9]. Electron ionization mass spectra of carboxylic acids, a linker in four of the five MOFs investigated here, show that decarboxylation and dehydroxylation are the first and most abundant fragmentation events [31]. Decarboxylation will free the metal center from the rigid framework, presumably releasing CO_2 and allowing metal-ion coalescence to occur. The aromatic ring component of the linker that remains is unlikely to further fragment, based on extensive literature showing that aromatic compounds are much more radiation resistant than aliphatic compounds [32, 33]. However, loss of the carboxyl groups will create aromatic radicals that can undergo polymerization and H_2 loss to form the carbonaceous material that surrounds the nanoparticles, some of which appears to be graphitic. This mechanism is quite different from nanoparticle formation in solution, where temperature, concentration, and identity of the reducing agent are important. It should also be noted that since carbon surrounds the nanoparticles, we cannot rule out the possibility of carbon contamination, which is observed in similar synthesis methods [33]. However, it is feasible to remove this contamination by annealing in air, as was shown previously for tungsten nanostructures [34].

We also expect that the ease of decarboxylation is correlated with the metal–linker bond strength and may influence the type of nanoparticle that forms. To determine the metal–ligand bond strengths of the various MOFs, we employed density functional theory (DFT) to estimate the homolytic bond dissociation energies in these MOFs. Specifically, we calculated the dissociation of a single linker within a MOF-like cluster (see supporting information available at stacks.iop.org/Nano/22/375601/mmedia) according to the reaction $(L)_n$–M–L $\rightarrow$ $(L)_n$–M$\cdot$ + L$\cdot$, where $(L)_n$–M–L refers to the cluster, $(L)_n$–M$\cdot$ is the remaining MOF radical fragment, and L$\cdot$ is the neutral linker radical. The calculations indicate that among the zinc-containing MOFs, the Zn–O bond in IRMOF-1 is the strongest, while the Zn–N coordination bond in ZIF-8 is the weakest. The Cu–COO bond energy in the Cu(BTC) cluster is also weak relative to IRMOF-1, which is consistent with its rapid degradation to form

Cu nanoparticles. The overall order of bond strength is ZIF-8 (2.3 eV) $\approx$ Cu(BTC) (2.5 eV) $\ll$ MOF-508 (4.5 eV) $<$ IRMOF-1 (5.4 eV) $<$ MIL-68(In) (6.0 eV). Although these values should not necessarily be taken at face value, the trend is not fully consistent with the observed rate and nanoparticle composition, suggesting that the geometry and composition of the coordination sphere are the key factors in determining particle composition and rate of formation. MIL-68(In) is the exception, having both a strong In–O bond and a rapid rate of e-beam breakdown. As a main-group element, we expect its oxides to be very stable, so its rapid decomposition in the electron beam to form metallic In nanoparticles may be the result of a unique combination of structural factors. Additional experiments will be needed to achieve a clear understanding of these effects.

In conclusion, our results demonstrate that metallic and semiconducting nanoparticles can be synthesized using electron beam irradiation of MOFs, using a TEM to monitor nucleation and growth in real time. Their type, size, and morphology are determined by the metal oxidation potential, coordination sphere, and e-beam current density and energy. Following MOF decomposition, the residual carbonaceous material provides a stabilizing matrix that prevents nanoparticle agglomeration and reoxidation of metallic nanoparticles. This method can be extended to MOFs with different linkers and metal centers, providing a versatile route to a variety of nanoparticle compositions, phases, and morphologies. Although the size of the exposed area in our proof-of-concept experiments was limited by the diameter of the TEM beam, high-resolution writing and broad-area exposure are possible using currently available instrumentation. When combined with the ability to infiltrate materials into the MOF pores prior to e-beam exposure, as we previously demonstrated with silver [8, 9], the potential to fabricate metallic and semiconducting nanoparticle heterostructures using MOFs as scaffolds or templates can be envisioned.

Acknowledgments

The authors thank Dr Joshua Sugar for his technical assistance with various aspects of this project. This work was supported by the Laboratory Directed Research and Development Program at Sandia National Laboratories. Sandia is a multiprogram laboratory operated by Sandia Corporation, a Lockheed Martin Company, for the United States Department of Energy's National Nuclear Security Administration under Contract DE-AC04-94AL85000.

Disclaimer. The full description of the procedures used in this paper requires the identification of certain commercial products and their suppliers. The inclusion of such information should in no way be construed as indicating that such products or suppliers are endorsed by NIST or are recommended by NIST or that they are necessarily the best materials, instruments, software or suppliers for the purposes described.

References

[1] Burda C, Chen X B, Narayanan R and El-Sayed M A 2005 *Chem. Rev.* **105** 1025
[2] Bronstein L M 2003 *Top. Curr. Chem.* **226** 55
[3] Mezhenny S, Lyubinetsky I, Choyke W J and Yates J T 1999 *J. Appl. Phys.* **85** 3368
[4] Luisier A, Utke I, Bret T, Cicoira F, Hauert R, Rhee S-W, Doppelt P and Hoffmann P 2004 *J. Electrochem. Soc.* **151** C535
[5] Della Ratta A D, Melngailis J and Thompson C V 1993 *J. Vac. Sci. Technol.* B **11** 2195
[6] Hermes S, Schroter M K, Schmid R, Khodeir L, Muhler M, Tissler A, Fischer R W and Fischer R A 2005 *Angew. Chem. Int. Edn* **44** 6237
[7] Moon H R, Kim J H and Suh M P 2005 *Angew. Chem. Int. Edn* **44** 1261
[8] Houk R J T, Jacobs B W, El Gabaly F, Chang N N, Talin A A, Graham D D, House S D, Robertson I M and Allendorf M D 2009 *Nano Lett.* **9** 3413
[9] Jacobs B W, Houk R J T, House S D, Robertson I M, Talin A A and Allendorf M D 2011 *Chem. Sci.* **2** 411
[10] Akcoltekin E, Peters T, Meyer R, Duvenbeck A, Klusmann M, Monnet I, Lebius H and Schleberger M 2007 *Nature Nanotechnol.* **2** 290
[11] Sepulveda-Guzman S, Elizondo-Villarreal N, Torres-Castro D F A, Gao X, Zhou J P and Jose-Yacaman M 2007 *Nanotechnology* **18** 335604
[12] Tanaka M, Chu F, Shimojo M, Takeguchi M, Mitsuishi K and Furuya K 2005 *Appl. Phys. Lett.* **86** 183104
[13] Wei X, Wang M-S, Bando Y and Golberg D 2010 *J. Am. Chem. Soc.* **132** 13592
[14] Shekhah O, Wang H, Strunskus T, Cyganik P, Zacher D, Fischer R and Woll C 2007 *Langmuir* **23** 7440
[15] Yaghi O M, O'Keeffe M, Ockwig N W, Chae H K, Eddaoudi M and Kim J 2003 *Nature* **423** 705
[16] Chen B L, Liang C D, Yang J, Contreras D S, Clancy Y L, Lobkovsky E B, Yaghi O M and Dai S 2006 *Angew. Chem. Int. Edn* **45** 1390
[17] Park K S, Ni Z, Cote A P, Choi J Y, Huang R D, Uribe-Romo F J, Chae H K, O'Keeffe M and Yaghi O M 2006 *Proc. Natl Acad. Sci. USA* **103** 10186
[18] Volkringer C, Meddouri M, Loiseau T, Guillou N, Marrot J, Ferey G, Haouas M, Taulelle F, Audebrand N and Latroche M 2008 *Inorg. Chem.* **47** 11892
[19] Chui S S Y, Lo S M F, Charmant J P H, Orpen A G and Williams I D 1999 *Science* **283** 1148
[20] Sawyer D T, Sobkowiak A and Roberts J L Jr 1995 *Electrochemistry for Chemists* (New York: Wiley)
[21] *ESTAR database Stopping powers and ranges for electrons* http://physics.nist.gov/PhysRefData/Star/Text/method.html National Institute of Standards and Technology web site, accessed Nov. 15, 2010
[22] Lee J J, Bang J and Yang H 2009 *J. Phys.* D **42** 025305
[23] Vanheusden K, Warren W L, Seager C H, Tallant D R, Voigt J A and Gnade B E 1996 *J. Appl. Phys.* **79** 7983
[24] Huang M H, Wu Y Y, Feick H, Tran N, Weber E and Yang P D 2001 *Adv. Mater.* **13** 113
[25] Jawhari T, Roid A and Casado J 1995 *Carbon* **33** 1561
[26] Balamurugan B, Kruis F E, Shivaprasad S M, Dmitrieva O and Zahres H 2005 *Appl. Phys. Lett.* **86** 083102
[27] Zhao M Q, Sun L and Crooks R M 1998 *J. Am. Chem. Soc.* **120** 4877
[28] Oshima Y, Nangou T, Hirayama H and Takayanagi K 2001 *Surf. Sci.* **476** 107
[29] Yokozeki A and Stein G D 1978 *J. Appl. Phys.* **49** 2224
[30] Reimer L 1989 *Transmission Electron Microscopy: Physics of Image Formation and Microanalysis* (Berlin: Springer)
[31] Martinez R I 1989 *J. Res. Natl Inst. Stand.* **94** 281
[32] Ferry M, Ngono-Ravache Y, Picq V and Balanzat E 2008 *J. Phys. Chem.* B **112** 10879
[33] Rightor E G, Hitchcock A P, Ade H, Leapman R D, Urquhart S G, Smith A P, Mitchell G, Fischer D, Shin H J and Warwick T 1997 *J. Phys. Chem.* B **101** 1950
[34] Sychugov I, Nakayama Y and Mitsuishi K 2009 *J. Phys. Chem.* C **113** 21516